Publications of the Astronomical Society of the Pacific, 132:055001 (9pp), 2020 May https://doi.org/10.1088/1538-3873/ab7a74

Charge Injection Device Performance in Low-Earth Orbit

D. Batcheldor[1], S. Sawant[1], J. Jenne[2], Z. Ninkov[3], S. Durrance[1], S. Bhaskaran[2], and T. Chapman[2]
[1] Aerospace, Physics & Space Sciences, Florida Institute of Technology, 150 West University Blvd, Melbourne, FL 32901, USA; dbatcheldor@fit.edu
[2] Thermo Scientific—CIDTEC, 101 Commerce Boulevard, Liverpool, NY 13088, USA
[3] Center for Imaging Science, Rochester Institute of Technology, 84 Lomb Memorial Drive, Rochester, NY 14623-5603, USA
Received 2020 January 31; accepted 2020 February 26; published 2020 March 18

Abstract

Charge Injection Devices (CIDs) have demonstrated direct contrast ratios in excess of 1:20 million from sub-optimal ground-based astronomical observations. CIDs are therefore interesting prospects for obtaining direct images from a host of high contrast ratio celestial scenes. However, while CIDs are capable of much deeper contrast ratios, potentially exceeding 1:1 billion, they do not address the Inner Working Angle (IWA) problem. If the Point-Spread Function (PSF) of a bright target is not well understood and accounted for, then the IWA will be large and nearby faint objects, like exoplanets, will be challenging to observe regardless of the detector used. As Earth's atmosphere is a major contributor to the variability of a PSF, high contrast ratio imaging with small IWAs will be best achieved in space. Therefore, if CIDs are to be used on future space-telescopes, they must be flight qualified in the space environment and shown to be at the appropriate Technology Readiness Level (TRL). Here we report the results of an 8 months CID technology demonstration mission that used the Nano-Racks External Platform mounted to the Kibo Exposed Facility on-board the *International Space Station*. Over the course of the 236 days mission we find no significant on-orbit changes of CID performance in terms of dark current, linearity, read noise, and photon transfer efficiency. As a result, CIDs are now space-qualified to TRL-8 and can be considered for future space telescopes.

Key words: instrumentation: detectors

Online material: color figure

1. Introduction

Exoplanets are now astronomical objects that can be studied in their own right. While early searches for exoplanets produced sporadic data (Wolszczan & Frail 1992; Mayor & Queloz 1995; Butler et al. 1999), more systematic radial velocity efforts have slowly grown the known number of exoplanets including possibly around Proxima (Anglada-Escudé et al. 2016; Damasso et al. 2020) and Barnard's Star (Ribas et al. 2018). However, it is the results from the *Kepler Space Telescope* (Borucki et al. 2008) that have provided the now large database of exoplanets necessary for more detailed studies (Borucki et al. 2011; Batalha et al. 2013; Burke et al. 2014). Following on from the limited field *Kepler* mission, the *Transiting Exoplanet Survey Satellite* (*TESS* Ricker 2016) has been successfully using the same transit technique to find the exoplanet systems of nearby stars across the whole celestial sphere (e.g., Huang et al. 2018; Nielsen et al. 2019; Vanderspek et al. 2019; Wang et al. 2019).

In both the radial velocity and transit methods the orbital inclination to our line of sight plays a major role in the detectability of exoplanet systems. This is not the case with direct imaging, but there are two major challenges with this approach. First, the contrast ratios between planets and their host stars are extreme. Second, the inner working angles (IWAs) necessary to spatially separate the planet from the star are incredibly small. However, should these two problems be overcome, a direct imaging survey of all nearby star systems is likely to reveal the presence of many more nearby exoplanets.

The compelling nature of exoplanetary science has sparked a number of techniques for maximizing contrast ratios and minimizing IWAs. For example, coronagraphy (Schneider et al. 2001), vortex coronagraphy (Foo et al. 2005), nulling interferometry (Linfield 2003), integral field spectral deconvolution (Sparks & Ford 2002), spectral differential imaging (Ingraham et al. 2012), angular differential imaging (Marois et al. 2006), space-based roll subtraction (Lowrance et al. 2005; Schneider et al. 2010), and fast focal plane wavefront sensing (Gerard et al. 2019). These techniques can be supplemented with software approaches such as Locally Optimized Combination of Images (LOCI) and Template LOCI (Lafrenière et al. 2007; Marois et al. 2014), as well as principal component analysis (Soummer et al. 2012, 2015). In each case, however, complications and costs arise from high wave-front quality requirements, the need for precise pointing control, additional support structures, and multiple apertures. In most cases, these approaches have been successful in detecting planets much larger than Jupiter at separations of tens of astronomical unit (Marois et al. 2010), or objects that turn out to be brown dwarfs (Konopacky et al. 2016).

At the heart of the contrast ratio (CR) problems are metal-oxide-semiconductor (MOS) arrays commonly used in optical and near-infrared astronomical imaging. These devices typically use standard 16 bit analog-to-digital converters producing an intrinsic limit of $\log(\mathrm{CR}) \gtrsim 5$ ($\Delta m \sim 12.5$). Exceeding this limit results in a persistence of signal in subsequence images or charges bleeding across pixels. However, one particular MOS array, the Charge Injection Device (CID), uses a 32 bit architecture that has the potential to reach $\log(\mathrm{CR}) = 9.6(\Delta m \sim 24)$. Batcheldor et al. (2016) demonstrated CID astronomical observations with $\log(\mathrm{CR}) = 7.3(\Delta m \sim 18.3)$. These observations were made without the costs and complications of the techniques mentions above; no special apertures or structures were needed, no wave-front corrections were made, and precise pointing control was unnecessary.

As encouraging as these results are, CIDs do nothing to reduce IWAs. Therefore, if CIDs are to be used as exoplanet imagers they must be part of a system that significantly suppresses and/or precisely models the point-spread function (PSF). Coupled with the need for very low backgrounds and high sensitivities, it becomes clear that CID systems will be most effective on space-based telescopes where PSFs are most stable. Until now, astronomical CIDs have only been tested using limited ground-based facilities. In terms of space-based operations, CIDs were therefore around Technology Readiness Level (TRL) 4 or 5 having been validated in an astronomically relevant environment.

Here we report on a successful 8 months mission in which a CID system was developed and demonstrated on board the *International Space Station* (*ISS*) consistent with TRL-8. In Section 2 we provide an overview of CIDs. In Section 3 we describe the *ISS* payload. Section 4 summarizes the mission operations. In Section 5 we present the results and analysis of the payload data. Section 6 discusses these results and the future of CIDs for space-based astronomy. Section 7 concludes.

2. Charge Injection Devices

CIDs are arrays of individually addressable MOS capacitor pixels separated by field oxide. As a result of the complex electronics necessary for individual pixel control early CIDs had read noise levels of $\sim 600e^{-}$ (McCreight & Goebel 1981; McCreight et al. 1986). This is one reason why CCDs were originally the preferred devices for astronomical applications. However, modern CIDs produce read noise levels comparable to CCDs because they include a pre-amplifier per pixel architecture, random access decoders, and a non-destructive read out (NDRO) approach (Eid 1995; Kimble et al. 1995; Batcheldor et al. 2016).

Each CID pixel contains a sense and a storage node. A zero-level read is made first. Charge holes are accumulated under the storage node then transferred within the pixel to the sense node. This signal is compared to the zero-level read. The charge holes are then either transferred back to the storage node (the integration continues non-destructively) or are injected back into the substrate. Post-injection the pixel restarts accumulating charge holes under the storage node without affecting the state of other pixels. CIDs are intrinsically anti-blooming, tolerant to changes in charge transfer efficiency, reject cosmic-rays through the NDRO process, and are radiation hard (Bhaskaran et al. 2008); they are appropriate candidates for space-based detectors.

Ninkov et al. (1994) initially demonstrated the viability of CIDs for astronomical imaging. Batcheldor et al. (2016) furthered these observations with a CID820. The CID820 used was a 2048×2048 12 μm pixel detector with linear response up to $268k\ e^{-}$ and a full well of $305k\ e^{-}$. The quantum efficiency was limited to 48% at 525 nm due to front illumination, the dark current was 5 $e^{-}\ \mathrm{s}^{-1}$ at -45.6 °C, and the read noise was 5.8 e^{-} rms with 128 NDROs.

A CID observation begins with a short (typically 0.1 s) pre-exposure to determine the most illuminated pixels. These bright pixels are assigned to a region of interest (ROI) before the science sequence begins. When 75% of the full well is reached the pixels in the ROI are read out and the charge holes subsequently injected to reset the pixel. Once the exposure is complete all pixels are read out and compiled with the data from the ROI. The ROI can be at any position on the detector so precise telescope pointing is not required to align a coronagraph with the bright source, for example.

The CID820 used by Batcheldor et al. (2016) required liquid cooling and bench mounted support hardware, and was installed on a 0.8 m ground-based telescope in Florida. Despite these limitations the CID820 achieved $\log(\mathrm{CR}) = 7.3(\Delta m \sim 18.3)$ by observing the Sirius field. As these observations did not have an instrument optimized for use on a telescope, nor a telescope located at an optimal observing site, these demonstrations validated CIDs as astronomical high-contrast imagers to only TRL-4/5.

3. The SpectraCAM Payload

Due to the required PSF stability for IWAs close to the diffraction limit, future CID based high-contrast astronomical observations will greatly benefit from being performed in space. However, to become part of an operational space-telescope, an actual CID system must be qualified for selection as a science instrument through successful demonstrations and testing (TRL-8). The SpectraCAM payload was therefore designed to test and demonstrate the space-based operations of a CID using the Nano-Racks External Platform (NREP) mounted to the Kibo Exposed Facility (EF) on-board the *ISS*.

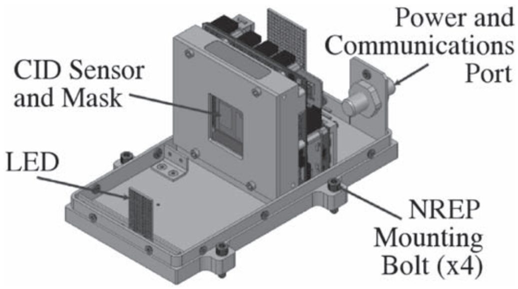

Figure 1. Internal layout of the SpectraCAM payload showing the major components inside a 2U CubeSat form factor.

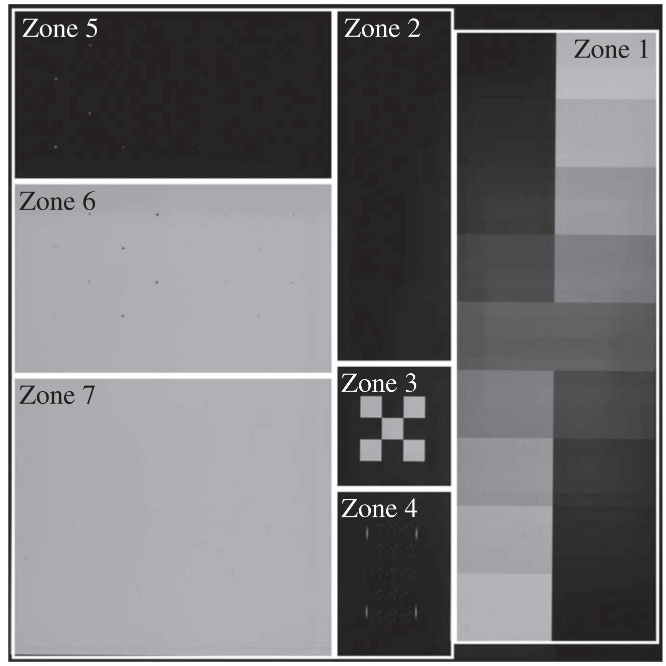

Figure 2. Layout of the mask zones used with the intent to gather multiple test data within one exposure overlaid on a pre-flight test image. More details are in the text. Zone 1: "grayscale." Zone 2: "Vernier." Zone 3: "contrast." Zone 4: "ICR." Zone 5: "star-field." Zone 6: "inverse star-field." Zone 7: "flat-field." A 74 pixel opaque border was present on all four sides.

The goals of the SpectraCAM mission were to quantify the on-orbit evolution of dark current and read noise, the response of the detector to an input illumination (linearity), the mean variance as a function of signal (photon transfer efficiency), and to demonstrate the radiation tolerance of a CID. The flight requirements of the payload were to: (1) be contained in a 2U CubeSat form factor, (2) operate in an ambient environment between -15 °C and 20 °C, (3) operate on less than 50 W, (4) communicate with the *ISS* via the STELLA command protocol, (5) store up to 3 days of data, (6) have a USB2.0 interface, and (7) produce minimal electromagnetic interference (EMI) from power and control lead conductive emissions between 30 Hz and 20 kHz (CE01, CE02), and magnetic field emissions between 30 Hz and 50 kHz (RE01).

Thermo CIDTEC, Inc. in Liverpool, NY constructed the SpectraCAM payload. Two systems were completed so that a mirrored data collection sequence could be carried out on the ground. Both the flight unit and ground unit were built using mainly using components-off-the-shelf. The aim was to maintain a sensor temperature of -20 °C, but the sensor temperature is not a requirement to reach TRL-8. The SpectraCAM payload was contained within an optically shielded black enclosure fitted with a sintered aluminum vent to allow out-gassing. The payload was not required to produce images of sources exterior to the enclosure. This removed the need for a gimbal, for tracking, or for any optical elements necessary to form a focus.

Figure 1 shows the internal layout of the SpectraCAM payload. A front-illuminated CID821, with a peak quantum efficiency of 40% at 555 nm, faced a 62.5 mW Kingbright APT1608SGC gallium phosphide green Light Emitting Diode (LED) with a peak wavelength of 565 nm, a bandwidth of 30 nm, and a viewing angle of 150°. The CID821 was supported by five stacked printed circuit boards: the Imager Specific Interface (ISI), a power board (PWR) to handle power regulation including a thermal electric cooler (TEC), a Freescale iMX6 800 MHx Quad Core-4 GB DDR3-1066 +32 MB Flash Camera Signal Processing (CSP) unit on two boards to control the LED, TEC, and sensor timing, and an interposer board to interface the ISI, CSP, and PWR boards. A heat sink ran through the base of the payload into the NREP for thermal management. Temperatures were recorded at the ISI, CSP, and PWR boards, and at the iMX6. A TMP431 was used for temperature monitoring with a remote diode integrated into the sensor.

With the intent of collecting multiple tests within one full-frame exposure, the 2048×2048 pixel sensor was masked into seven zones. A test pattern was etched into a chrome plated glass window placed approximately 1 mm in front of the sensor. Figure 2 demonstrates the layout of the zones created using varying transparencies of the mask. Originally, Zone 1 ("grayscale") was designed to probe the photoresponse of the detector, Zone 2 ("Vernier") was designed to map the mask coordinates to pixel positions, Zone 3 ("contrast") was designed to provide maximum contrast between adjacent zones, Zone 4 ("spectra") was designed to mimic spectral emission lines, Zone 5 and 6 were designed to mimic star-fields, and Zone 7 was designed to provide a large area over which the on-orbit evolution in the detector efficiency could be investigated. Ultimately, the data generated from this mask was not used to support the development of this sensor to TRL-8. Instead, all tests were performed in a small 100×100 sub-array test location described in Section 5.

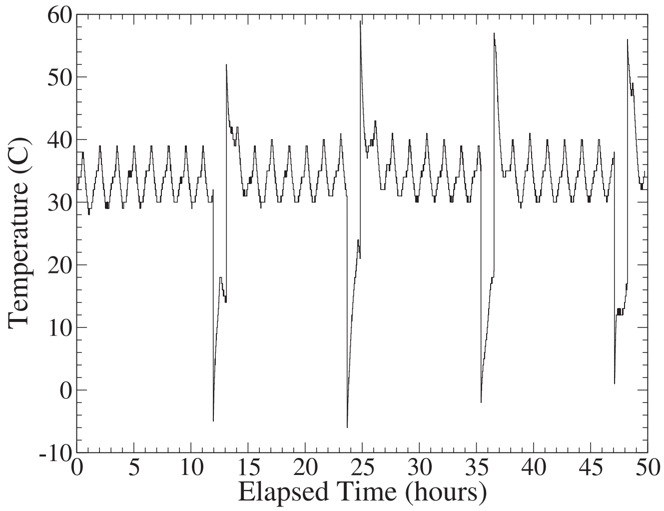

Figure 3. Temperature variations of the sensor in one second intervals beginning MD006 (2017 May 3rd). The *ISS* orbital period is demonstrated in the 10 °C temperature variations every 1.5 hr. A signifiant drop every 12 hr corresponds to the TEC power on. The sharp increase in temperature after the TEC is turned on indicates thermal runaway within the payload.

4. Mission Summary

The SpectraCAM flight unit successfully demonstrated the operational requirements for EMI. It was then delivered to NanoRacks for payload integration on 2016 September 23rd and launched on SpaceX CRS-10 on 2017 February 19th. The payload was installed onto the NREP, deployed to the EF, and successfully powered up on 2017 April 28th. Final power down occurred after 236 days on 2017 December 20th. SpectraCAM was removed from the NREP on January 4th and temporarily stowed before departing *ISS* on the SpaceX-14 Dragon capsule that splashed down 2018 May 5th. The payload was received by the NanoRacks Houston office on 2018 June 28th and then forwarded to ThermoFisher in Liverpool, NY.

Between Mission Days zero and four (MD000–MD004), corresponding to 2017 April 28th to May 1st, 7 test data sets were acquired every 12 hr with the TEC power off. This resulted in an average sensor temperature of 29 °C at the beginning of the tests. Between MD004 and MD021 the TEC was powered on one hour before the data acquisition tests were executed. The data were then saved before the TEC was powered off.

Figure 3 demonstrates the temperature variations of the sensor in one-second intervals beginning MD006 (2017 May 3rd) and lasting 50 hr across four data sets. The temperature variations recorded at the sensor were also seen at the ISI, CSP, and PWR boards, with constant offsets of 41 °C, 60 °C, and 46 °C, respectively. The *ISS* orbital period is easily seen in the cyclical day–night temperature variations every 1.5 hr, and 37 °C drops are seen every 12 hr corresponding to when the TEC is powered on. Due to the 10 °C variations in payload temperature from the day–night environment, the sensor was not brought to the same initial temperature by the TEC at the start of each data set. Instead the sensor temperature dropped below the ambient payload temperature based on the *ISS* orbital position in direct sunlight or Earth's shadow. The sensor is also seen to warm significantly during the initial hour after the TEC was powered on. These temperature increases are larger than those occurring due to the day–night variations.

Between MD004 and MD021 a total of 36 data sets were acquired with the sensor ranging from 4.9 °C to 23.5 °C with an average of 13 °C at the beginning of the test sequences. This was outside the design requirements of -20 °C. During MD021 the NREP power failed. Once power was re-established, 41 further data sets were collected with 12 hr intervals between MD024 and MD044. In this case the sensor temperature ranged from 0.5 °C to 18.9 °C with an average of 9.3 °C. This was still outside the design requirements of -20 °C.

On MD046 (2017 June 13th) NREP experienced another failure and automatically rebooted. Once communications with the SpectraCAM were re-established it was found that no new files had been stored since MD044. A flash storage issue was discovered and worked-around put in place. A portion of the RAM was made available as a non-persistent small file-system and the in-orbit FTP server was used to transfer the data out of the SpectraCAM as soon as possible after each acquisition. The new firmware created for this workaround also reduced the time between the TEC being powered on and the beginning of the data collection. Now only 2 minutes, this shortened TEC timing significantly reduced the average sensor temperature during the data acquisition; the previous 1 hr TEC timing was causing the payload to experience thermal runaway (Figure 3).

Two minutes after the TEC was powered on a global charge inject was performed and the entire array non-destructively read. A full-frame image was then collected with the LED providing illumination. To stabilize its output the LED was flashed on and off every 30.72 ms. This on-off flash sequence was repeated 20 times for a total of 1.2 s, after which the entire array was non-destructively read again. Following the full-frame read the linearity test was performed. A 100×100 sub-array was defined in Zone 7 and read 201 times after a global inject. The LED flash sequence was set to 480 ms and repeated 20 times per read. The same sub-array was used to sample the dark current 201 times after a global inject. The linearity and dark current data were collected over 192 s each. The read-noise was also sampled from the sub-array after 1, 2, 4, 8, 16, and 32 NDROs each after a global inject. Finally, the sub-array was used to measure the mean variance as a function of signal, i.e., the photon transfer curve (PTC). Using 51 different LED illuminations with a 240 ms flash cadence, this final test took 245 s. Combining all tests each 12 hr data acquisition was completed over approximately ten minutes.

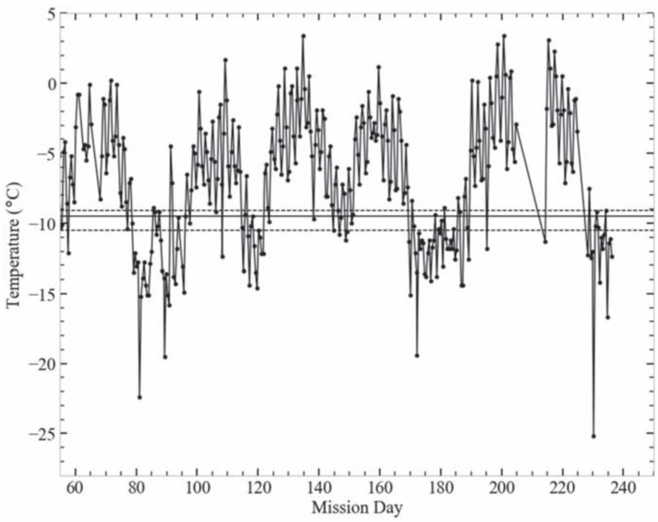

Figure 4. Post-firmware upgrade temperature variations of the sensor at the beginning of the full-frame tests. The horizontal solid black line is the average sensor temperature of the ground unit, with the dashed lines indicating the upper and lower limits.

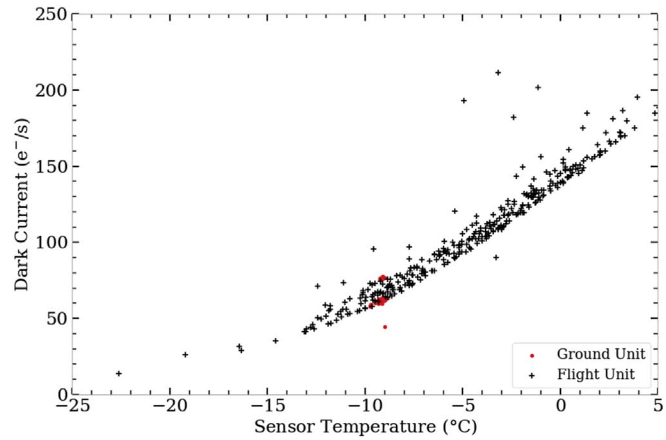

Figure 5. Dark current as a function of sensor temperature for both the flight unit (black points) and ground unit (red points).

(A color version of this figure is available in the online journal.)

MD054 (2017 June 21st) marked the beginning of a period of stable data collection, with losses only occurring on MD065 and MD066. Between MD054 and MD204 294 data sets were acquired every 12 hr. The end of 2017 October marked 6 months of on-orbit operations, but the SpectraCAM remained collecting data until a final power down of the NREP was required for new payloads to be installed. Therefore, a further 38 data sets were collected between MD213 and MD236 (2017 December 20th). Over the entire 236 days mission a total of 502 data sets were acquired.

After the firmware updates there were 332 data sets where the sensor temperature ranged at the beginning of a data acquisition sequence from −25.2 °C to 3.4 °C with an average of −7 °C (Figure 4). This was an improvement over the original TEC power process but still generally outside the sensor temperature requirements of −20 °C (the sensor temperature requirement were only met by four data sets). By the end of the data acquisition sequence, following the PTC test, the average sensor temperature rose by 6.7 °C.

The ground unit was operated with the new firmware and the TEC provided comparable sensor temperatures to those being achieved by the flight unit. Between 2017 June 29th and 2018 March 6th a total of 436 data sets were acquired very 12 hr with the sensor temperature at the beginning of the full-frame tests ranging from −10.5 °C to −9.1 °C with an average of −9.5 °C. The ground-unit data are given in Figure 4 as the horizontal solid and dashed lines. By the end of the PTC test, the ground unit average temperature had risen by 0.8 °C.

5. Results

The results presented are derived only from data collected after the firmware update between MD054 and MD236. Figure 5 demonstrates the flight and ground unit dark current as a function of the sensor temperature during the version 2 firmware period. The dark currents are within the range of those expected for the CID821. Due to the significant temperature increase differences between the flight unit and ground unit during the data acquisition, it was necessary to extract the average sensor temperatures between the beginning and end of the dark current test. The relative stabilities and swings of the flight unit and ground unit temperatures are clear in Figure 5, and are expected due to the day–night orbital temperature variations demonstrated in Figure 4. However, for a given sensor temperature the ground and space unit CIDs demonstrated no significant differences in the dark current.

Figure 6 is a stretched image of an example full-frame to highlight the contrast across the sensor. This example is from on-orbit data collected on MD144 at a sensor temperature of −7.2 °C corresponding to the average sensor temperature recorded after the firmware update. In Zone 1 structures can be seen to result from the stacking of at least twelve mask images generated by reflections internal to the payload. Such reflections are attributed to the payload enclosure and the glass window onto which the mask itself was etched. Discrete specks are also seen in Zone 7 and some sub-zones within Zone 1. Such specks, but in different positions, were also noted in pre-flight test images and are attributed to the flaking of excess thread-locker used on the enclosure mounting bolts (Loctite #243 and #7649 primer). These flakes were found upon inspection of the payload interior post-flight. It was also noted that the mask positioning shifted between pre-flight and EF

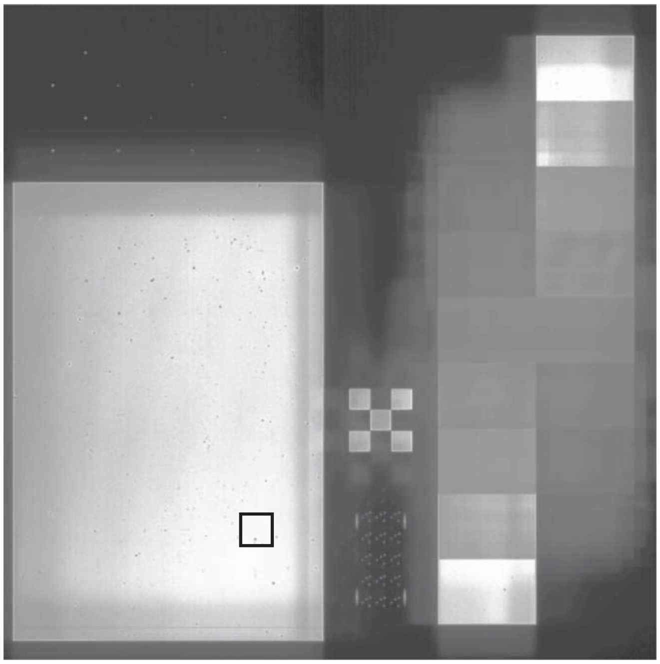

Figure 6. A stretched full-frame to highlight structures resulting from internal reflections and debris on the mask window. The black square highlights the position of the 100 × 100 sub-array test location in Zone 7.

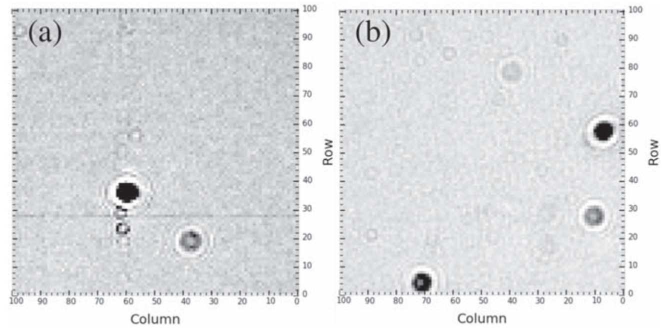

Figure 7. The 100 × 100 sub-array test locations in detail for the flight (a) and ground (b) units. The spots are attributed to Loctite flakes. Within these regions there were no variations due to internal reflections.

deployment. Such shifts are expected from launch stresses and the weightless environment.

Figure 7 shows in greater detail the structure in the 100 × 100 sub-array test regions from both the flight unit (a) and ground unit (b). The Loctite specks are clearly seen and did not move position while the flight unit was collecting the test data. In addition, there are no impacts on these regions from the internal reflections. Thus any variations in test-area derived data can be exclusively attributed to a change in the sensor performance.

As *ISS* orbited, day–night temperature variations in LEO impacted the overall payload temperature. Consequently, when the TEC was turned on, the initial sensor temperature varied from data set to data set with the performance of the sensor varying accordingly. Figure 8, top and bottom respectively, shows the impact of these temperature variations on the dark current and linearity. In order to highlight any long-term trends in these temperature driven data sets from the flight unit, a low-pass filter was applied in the form of a running average. For the post-firmware update, an average over 66 data points produced five separate bins of the flight unit data. However, regardless of linear least-squares fits to the binned or un-binned data, there was no difference in overall performance between the flight unit and ground unit.

Due to the impact of the flight-unit temperature variations, direct comparison with the ground-unit data have been made in the cases when the flight-unit sensor temperatures were consistent with the ground-unit temperatures. Figure 9 summarizes the flight unit performance as compared to the ground unit for read noise, dark current, linearity, and photon transfer efficiency as the mission progressed. The differences between the flight unit and ground unit linearity tests are a result of 50% shorter LED flash times on the ground unit. Linear fits to the data demonstrate that both units are consistent with no degradation in performance over the mission lifetime.

Data sets taken during a transit through the South Atlantic Anomaly were identified and compared to the average performance of the sensor. No significant differences were found. In addition, there was no significant increase in the number of dead pixels over the mission lifetime. These findings demonstrate this payload was radiation hard (e.g., Bhaskaran et al. 2008).

6. Discussions

Based on fits to the data from the flight unit, as compared to data from the ground unit, there is no loss of performance for a CID when operating in LEO. Consequently, the SpectraCAM payload and mission described here has successfully demonstrated and tested a complete CID imaging system in the space environment consistent with the NASA TRL-8.

The thermal management of the SpectraCAM limited its ability to achieve the original sensor temperature goals, and this impacted the absolute performance of the CID particularly in terms of the measured dark current. In addition, as the mission design did not go up to 128 NDROs, and was instead limited 32 NDROs, the read noise measured was significantly higher than could have been achieved. However, the goal of this mission was to demonstrate the impact of the space environment rather than the absolute CID performance previously demonstrated on the ground.

The Loctite debris on the detector window is another payload feature that can be mitigated in future space-based CID detectors. This debris had no impact on the demonstration of the CID in LEO, but would have been an inconvenience had

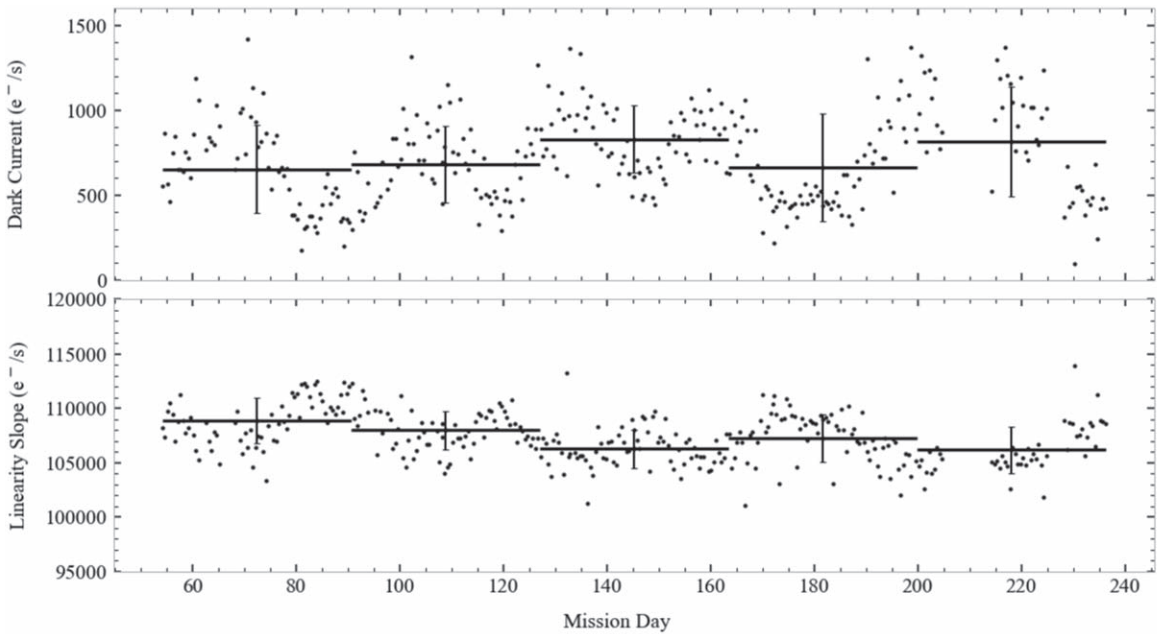

Figure 8. Full flight-unit data sets for (top) dark current and (bottom) linearity. The variations seen in these data are a result of the day–night temperature swings in LEO. A running average was applied as a low-pass filter to highlight any long term trends in performance as demonstrated by the solid lines. The data are consistent with no change in sensor performance.

the goals been to carry out high quality imaging of scenes external to the payload.

The intent of the chrome mask was to enable a variety of complex tests of the CID using a minimum of individual images. The data from these mask zones could be used for further testing of the detector, but in terms of the mission goals the data from the 100 × 100 sub-array test location proved adequate. A smaller CID array could have therefore been used in this payload to achieve the missions goals, potentially with better thermal management and an increased number of NDROs. However, it was a 2048 × 2048 pixel detector that was available at the time, and so the opportunity to gather more data was taken rather than to potentially compromise the mission timeline having to wait for a smaller array and a redesign of the payload.

As we move into the era of the next great space-observatories, with the recently completed design studies of LUVOIR (The LUVOIR Team 2019), Habex (Gaudi et al. 2018), Lynx (The Lynx Team 2018), and OST (Meixner et al. 2019) being produced for the 2020 Decadal Survey, it is clear that the main instrumentation interests of the astronomical community are in large, complex, long-term, expensive missions still with significant technology gaps. However, with CIDs being demonstrated as relevant to many of the goals of these large missions, perhaps there are smaller, faster, and cheaper ways of pushing the field of astrophysical high-contrast ratio imaging forward.

CIDs alone, while now demonstrated to operate in the space environment, will not reach the kinds of IWAs necessary for exoplanet imaging. Consequently, to meet the requirements set forth by these objects, a potential next step for CIDs is for them to be integrated with relatively simple observing techniques, like azimuthal differential imaging, and software based PSF modeling techniques. It is therefore worthwhile to conduct mission design concepts for small space telescopes that could potentially be launched as secondary payloads. Such a design study could demonstrate that the next logical step to *TESS* is a small space telescope capable of directly imaging a sample of exoplanets around the nearest stars.

7. Conclusions

There are a host of fundamentally important astronomical objects that present challenges to current technologies in terms of their achievable contrast ratios. Many complex, difficult, and expensive techniques have been developed in order to meet these challenges with a range of success. CIDs do not suffer from many of the issues that limit the contrast ratio capabilities of other detectors, and they are potentially a simple and relatively cheap way of approaching the study of high contrast astronomical scenes. However, until recently, CIDs had not been demonstrate in the space environment where their abilities could be made best use of due to stable PSFs. As a result of this work, however, a CID payload was developed and demonstrated on the *ISS*. During the course of this mission there was

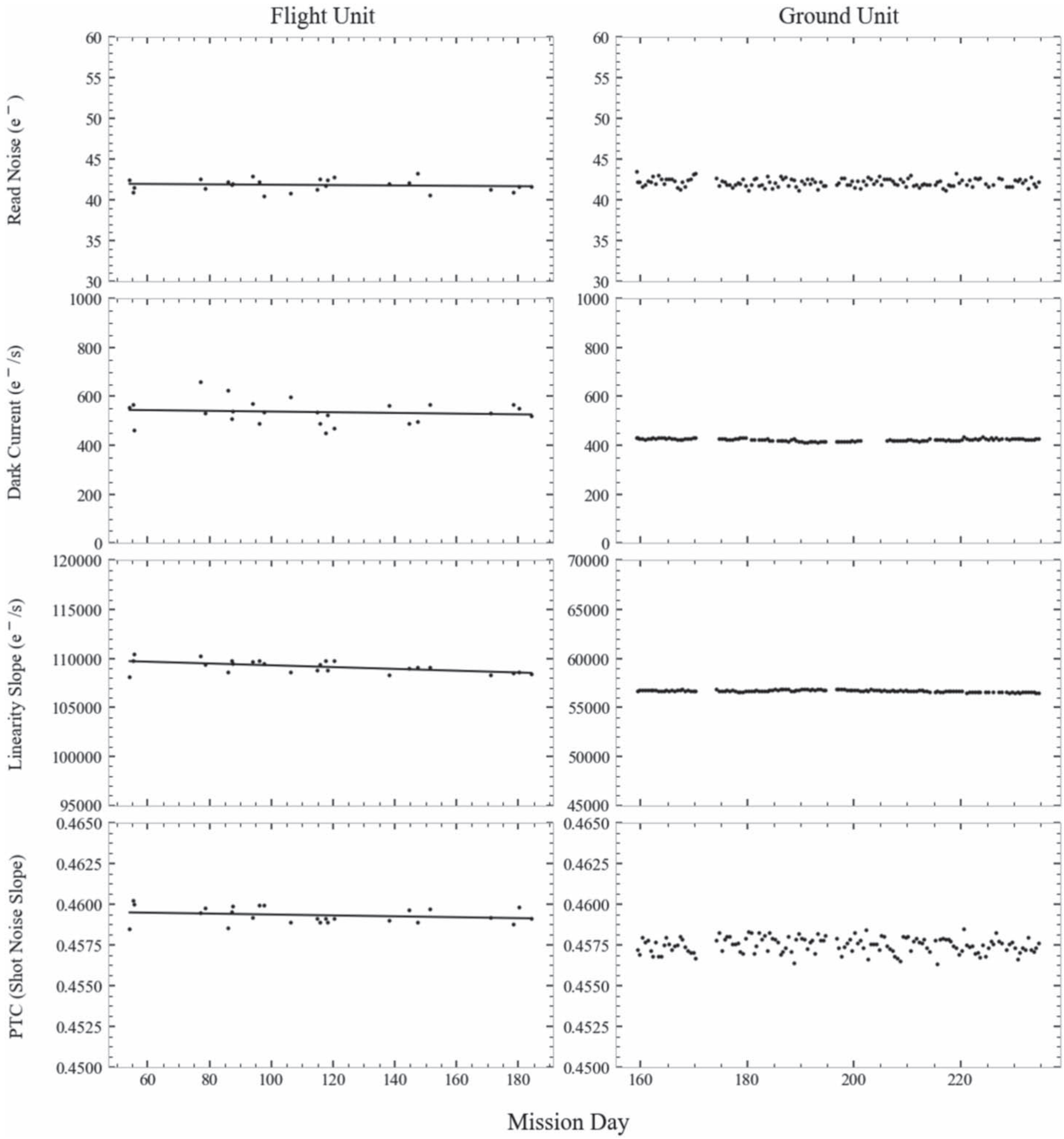

Figure 9. Read noise, dark current, linearity, and photon transfer curve (PTC), as a function of Mission Day, for the (left) flight unit and (right) ground unit when the two units reported consistent sensor temperatures. Linear fits to the flight-unit data are the solid lines and are consistent with no change in the sensor performance.

no degradation of the detector performance. As a consequence, we conclude the CIDs are now qualified to TRL-8 and should be considered for future space instruments that have the goals of high-contrast ratio direct imaging.

The authors gratefully acknowledge financial support from the Center for the Advancement of Science in Space (CASIS) GA-2014-141 for this study. The authors are also thankful for the support of NanoRacks and SpaceX. D.B. also wishes to thank the anonymous referee for comments and suggestions that improved the quality and clarity of this paper.

ORCID iDs

D. Batcheldor https://orcid.org/0000-0002-8588-5682

References

Anglada-Escudé, G., Amado, P. J., Barnes, J., et al. 2016, Natur, 536, 437
Batalha, N. M., Rowe, J. F., Bryson, S. T., et al. 2013, ApJS, 204, 24
Batcheldor, D., Foadi, R., Bahr, C., et al. 2016, PASP, 128, 025001
Bhaskaran, S., Chapman, T., Pilon, M., & VanGorden, S. 2008, Proc. SPIE, 7055, 70770RB
Borucki, W., Koch, D., Basri, G., et al. 2008, in IAU Symp. 249, Exoplanets: Detection, Formation and Dynamics, ed. Y.-S. Sun, S. Ferraz-Mello, & J.-L. Zhou, 17
Borucki, W. J., Koch, D. G., Basri, G., et al. 2011, ApJ, 736, 19
Burke, C. J., Bryson, S. T., Mullally, F., et al. 2014, ApJS, 210, 19
Butler, R. P., Marcy, G. W., Fischer, D. A., et al. 1999, ApJ, 526, 916
Damasso, M., Del Sordo, F., Anglada-Escudé, G., et al. 2020, SciA, 6, eaax7467
Eid, S. I. 1995, Proc. SPIE, 2415, 292
Foo, G., Palacios, D. M., & Swartzlander, G. A., Jr. 2005, OptL, 30, 3308
Gaudi, B. S., Seager, S., Mennesson, B., et al. 2018, arXiv:1809.09674
Gerard, B. L., Marois, C., Galicher, R., et al. 2019, arXiv:1910.04554
Huang, C. X., Burt, J., Vanderburg, A., et al. 2018, ApJL, 868, L39
Ingraham, P., Doyon, R., Lafrenière, D., & Beaulieu, M. 2012, PASP, 124, 454
Kimble, R. A., Chen, P. C., Haas, J. P., et al. 1995, Proc. SPIE, 2518, 397
Konopacky, Q. M., Rameau, J., Duchêne, G., et al. 2016, ApJL, 829, L4
Lafrenière, D., Marois, C., Doyon, R., Nadeau, D., & Artigau, É. 2007, ApJ, 660, 770
Linfield, R. P. 2003, Proc. SPIE, 4852, 443
Lowrance, P. J., Becklin, E. E., Schneider, G., et al. 2005, AJ, 130, 1845
Marois, C., Correia, C., Véran, J.-P., & Currie, T. 2014, in IAU Symp. 299, Exploring the Formation and Evolution of Planetary Systems, ed. M. Booth, B. C. Matthews, & J. R. Graham (Cambridge: Cambridge Univ. Press), 48
Marois, C., Lafrenière, D., Doyon, R., Macintosh, B., & Nadeau, D. 2006, ApJ, 641, 556
Marois, C., Zuckerman, B., Konopacky, Q. M., Macintosh, B., & Barman, T. 2010, Natur, 468, 1080
Mayor, M., & Queloz, D. 1995, Natur, 378, 355
McCreight, C. R., & Goebel, J. H. 1981, ApOpt, 20, 3189
McCreight, C. R., McKelvey, M. E., Goebel, J. H., Anderson, G. M., & Lee, J. H. 1986, Proc. SPIE, 686, 66
Meixner, M., Cooray, A., Leisawitz, D., et al. 2019, arXiv:1912.06213
Nielsen, L. D., Bouchy, F., Turner, O., et al. 2019, A&A, 623, A100
Ninkov, Z., Tang, C., Backer, B., Easton, R. L., & Carbone, J. 1994, Proc. SPIE, 2198, 868
Ribas, I., Tuomi, M., Reiners, A., et al. 2018, Natur, 563, 365
Ricker, G. R. 2016, AGUFM, P13C-01
Schneider, G., Becklin, E. E., Smith, B. A., et al. 2001, AJ, 121, 525
Schneider, G., Silverstone, M. D., Stobie, E., Rhee, J. H., & Hines, D. C. 2010, in Hubble after SM4. Preparing JWST, ed. S. Deustua & C. Oliveira (Baltimore, MD: STScI)
Soummer, R., Choquet, E., Pueyo, L., et al. 2015, AAS Meeting, 225, 349.21
Soummer, R., Pueyo, L., & Larkin, J. 2012, ApJL, 755, L28
Sparks, W. B., & Ford, H. C. 2002, ApJ, 578, 543
The LUVOIR Team 2019, arXiv:1912.06219
The Lynx Team 2018, arXiv:1809.09642
Vanderspek, R., Huang, C. X., Vanderburg, A., et al. 2019, ApJL, 871, L24
Wang, S., Jones, M., Shporer, A., et al. 2019, AJ, 157, 51
Wolszczan, A., & Frail, D. A. 1992, Natur, 355, 145